J A S T
Journal of Aerospace Science and Technology

# A Comparison of Smart and Conventional Flaps Close to Ground on Aerodynamic Performance

**M. H. Djavareshkian[1], A. Esmaeli[2] and A. Parsania[3]**

The prediction of aerodynamic characteristics and the smart flap of airfoil under the ground effect have been carried out by the integration of computational fluid dynamics. Considering different types of beams, a parametric bending profile of a smart flap is designed. A cantilever beam with uniformly varying load along with roller support at the free end is considered here. A pressure-based implicit procedure is utilized to solve Navier-Stokes equations and a nonorthogonal mesh with a collocated finite volume formulation is used to simulate. The boundedness criteria for this procedure are determined by the Normalized Variable Diagram (NVD) scheme. The procedure incorporates the $k - \epsilon$ eddy-viscosity turbulence model. The SIMPLE algorithm is applied for turbulent aerodynamic flows around airfoil with smart and conventional flaps. The results of two flaps are compared for different flap length, flap angle and ground clearance. It is found that: 1- The pressure coefficient distribution in the smart flap is smoother than that of the conventional flap; 2- The lift-drag ratio in the smart flap is higher than that of the conventional flap; 3- The maximum lift-drag ratio is at flap angle 7.5°; 4- The minimum ground clearance has the highest lift-drag ratio; and 5- The increasing of flap length leads to an increase in the lift-drag ratio.

## NOMENCLATURE

| | |
|---|---|
| $A$ | Cell Face Area |
| $AOA$ | Angle of Attack |
| $AOF$ | Angle of Flap |
| $B$ | Length of the Beam |
| $c$ | Cord Length |
| $CD$ | Drag Coefficient |
| $CF$ | Conventional Flap |
| $CL$ | Lift Coefficient |
| $D$ | Drag Force |
| $E$ | Young's Modulus |
| $F$ | Mass Flux |
| $h$ | Ground Clearances |
| $I$ | Flux |
| $\kappa$ | A factor in SBIC scheme to determine a special scheme |
| $L$ | Lift Force |
| $P$ | Pressure |
| $\vec{q}$ | Scalar Flux Vector |
| $Re$ | Reynolds Number |
| $SF$ | Smart Flap |
| $\vec{S}$ | Source Term |
| $\vec{V}$ | Velocity Vector |
| $X$ | Horizontal Cartesian Coordinate |
| $Y$ | Vertical Cartesian Coordinate |
| $\delta v$ | Cell Volume |
| $\phi$ | Scalar Quantity |
| $\Gamma$ | Diffusivity Coefficient |
| $\rho$ | Density |
| $\bar{I}$ | Area moment of inertia($\mathrm{m}^4$) |

3. *Finite Difference Method*
4. *Finite Element Method*
5. *Finite Volume Method*
1. *(Corresponding Author), Associate Professor, Dept. of Mech. Eng., Ferdowsi University Of Mashhad, Mashhad, Iran.*
2. *Dept. of Mech. Eng., Ferdowsi University Of Mashhad, Mashhad, Iran.*
3. *Dept. of Mech. Eng., Ferdowsi University Of Mashhad, Mashhad, Iran.*

| $\omega_0$ | Weight/Unit Length(N/m) |
| $\bar{\phi}$ | Normalized Scalar Quantity |
| $\mu$ | Dynamic Viscosity |
| $T$ | Time |
| $\vec{T}$ | Stress Tensor |

### INTRODUCTION

One of the most important goals in the development of a transportation system is its economic efficiency. Today, the time of transporting passengers and cargo becomes an eminent factor when assessing the economic viability of the means of transportation. Also, it is prominent in the reduction of fuel consumption and increasing the efficiency of transportation vehicles. There are different ways for increasing efficiency. One of them is using ground effect. The transportation system utilizing ground effect is expected to become one of high speed and enough efficiency. Wing-in-ground-effect (WIG) vehicles are very efficient, which help to increase the flight range at reduced specific fuel consumption in comparison with the conventional aircraft, trains and ships. This is accomplished happen when a wing is goes near the surface. As the mass flow and height under the airfoil is decreased, pressure begins to build on the lower surface of the airfoil. Hence, air cushion is created by the high pressure that it builds up under the wing and causes an increase in lift force and reduction in drag force. The information about the effects that ground can have on airfoils dates back to the early 1920s.

In recent years, there have been successful investigations on the aerodynamics of airfoil and wing. One of the most recent wind tunnel experiments was performed by Ahmed and Sharma [1, 2]. They have investigated the effect of variation of angle of attack and ground clearance on aerodynamic characteristics in a symmetrical airfoil. This study was conducted by using a fixed and moving ground plane in a wind tunnel [3]. The water tunnel investigation of pairs of vortex filaments in ground effect has been done by Kliment and Rokhsaz [4]. The investigation of unsteady varying of ground clearance has been performed by Matsuzaki et.al. [5]. Zerihan et.al. [6] have tested the aerodynamic behavior of a cambered single element, high-lift wing in ground proximate in wind tunnel. Ogurek et.al. [7] have carried out various sizes of winglet designs for a wing both in and out of ground effect. The aerodynamic characteristics of NACA6409 in ground proximity have tested by Jung et.al. [8]. They have surveyed the influence of the aspect ratio of wing, endplate and its shape in different angles of attack and ground clearnce. Smith [9] and Smith et.al. [10] have performed the computational analysis of airfoils in ground effect. Patrick Vu [11] has studied wing tip

vortices in inverted airfoils close to the ground, which are used in racing cars. The influence of endplate on aerodynamic characteristics for a low-aspect-ratio wing in ground effect was carried out by Park and Lee [12]. Abramowski [13] has presented a numerical study of NACA/Munk M15 airfoil in ground proximity. Moon et.al. [14] have simulated three-dimensional wings in ground effect for an aero-levitation electric vehicle. The numerical optimal design of a wing in-ground-effect craft was done by Kim et.al. [15]. Park et.al. [16] have offered optimization of airfoils under ground effect. The effect of ground proximity on the aerodynamic performance and stability of a light unmanned aerial vehicle have been performed by Boschetti et.al. [17]. The shape optimization by using the multi-objective genetic algorithm and the analysis of the 3-dimensional wings in ground effect was carried out by Juhee et.al. [18].

Flaps can be utilized to increase lift to drag ratio. They add efficiency and energy savings. Zerihan et.al. [19] have performed a computational study in order to model the flow around a double element airfoil in ground effect. Several authors have studied the possible exploitation of unsteady flapping in ground effect. [20, 21] Notably, Jones et.al. [21] have explored novel flapping propulsion techniques mimicking ground effect or mirror plane approaches by using 2-dimensional airfoils. Willis et.al. [22] have examined the ground effect phenomenon in flapping flight and they have determined the general rules which might aid in the design of MAV's and UAV's by utilizing both flapping and ground effect strategies. Kamali and Rezaei Ravesh [23] have investigated a numerical analysis of MAV's flapping wing in unsteady conditions.

In all of the aforementioned studies, conventional airfoil and wing is applied, but new materials exist now. Hence, they can be used to enhance efficient vehicles in ground effect. Although smart material technology was introduced about 10 years ago, it has widely developed and it has been utilized in different fields. New smart material technology in the aerospace industry was first introduced in 1969. More than one million of these joints have been applied in military aircraft since 1969. Therefore, due to the potential benefits of employing adaptive airfoils, there has been an intensive attempt by researchers in developing a working model. With the advancement of materials, smart materials are now considered to produce airfoil with variable camber capability. An analytical study on the benefits of variable-camber capability was conducted by NASA [24]. Another advantage of adaptive airfoil is that generated vortex is smaller and it has less power. This is the result of Pern and Jacob's [25] research. They have utilized piezoelectric stimulus with a steel layer in an airfoil. In 1997, Kudva et.al. [26] inquired about smart structure technologies and their

benefits. In 2003, Forster *et.al.* [27] designed a two-dimensional airfoil with a control surface in trailing edge that had chord wise geometrical changes. In 2003, a joint project was carried out the field of smart wing applications by a US aerospace research center (NASA) and a German aerospace research center (NGC) [28]. Recently, a multi blade fan with smart a material (memory alloy) has been built in such a way that its intake can be varied by electrical stimulation [29]. Another benefit of using smart materials is reducing vibration of helicopter blades [30]. The noise produced by airplanes and helicopters can be reduced by smart materials [31]. In 2010, Barlas *et.al.* [32] proposed a new idea in applying smart technology in wind turbine. The other way of utilizing smart materials in airfoils is that flap ribs can be made of smart materials such as piezoelectric or memory alloy. That is what is carried out in 2005 by Campanile and Anders [33]. Chinnasamy *et.al.* [34] asseyed the aerodynamic coefficients. Matsuzaki and Torii [35] predicted flutter in smart wings. Smart material could be used as wing skins. These wings are called flexible wings. Majji *et.al.* [36] examined a flexible three dimensional wing. Abdullah and Watkins [37] succeeded in making adaptive airfoils by appling shape memory alloy (NiTi) and flexible skins. Wickramasinghe *et.al.* [38] made a flight device with ribs by piezoelectric fiber. Abdullah *et.al.* [39] studied an adaptive airfoil system by utilizing Shape Memory Alloy (SMA) Actuators with a wind tunnel test.

Smart materials have not been applied since the appearance of ground effect vehicles. In this paper, an innovative idea is sugested. The innovation is first introduced in ground effect vehicles in the world per current authors. The effect of smart wings in ground effect has been assessed in none of the above-mentioned studies. To improve the advantage of aerodynamic coefficient, a smart wing can be used near the ground. Smart technology can create an evolution in the aerodynamics of ground effect vehicles.

The aim of this research is to investigate the smart and conventional flap in ground effect. Thus, the effect of flap angle, flap length and ground clearance on an airfoil has been examined in smart and conventional flaps. The comparison of smart and conventional flap is performed as well.

## SMART MATRIAL
The meaning of "SMART MATRIAL" in the material world has dramatically changed since 1992, when "SMART MATRIALs" was commercially used for the first time. It is now defined as highly engineered materials that respond to their environment intelligently. Smart materials have become the 'go-to' answer for the 21st century's technological needs. Smart materials are materials which possess the capability to sense and actuate in a controlled way in response to variable ambient stimuli. Generally, the known types of smart materials are ferroelectric materials (piezoelectric, electrostrictive, magnetostrictive), variable rheology materials (electro rheological, magneto rheological) and shape memory alloys (SMA). Piezoelectric materials and shape memory alloys are generally the most famous smart materials used in actuators in various applications. The development of their technology has reached a quite high level so that commercial solutions are available now and they are widely used. Smart material actuators comprise one of the most important parts of active control.

## NUMERICAL SOLUTION SETUP AND ITS CONDITIONS
### A: Simulation smart flap deflection
In this study, smart flap deflection is designed with a cantilever beam so that the beam bending equation is the same smart flap chord deflection. Since the flap shape is a triangle, the cantilever beams with a uniformly varying load are considered in Figure 2. The same profile is also used by Djavareshkian *et.al.* [39]. The above-mentioned profile is given below:

$$Y = \frac{w_0(-X^5 + 2B^2X^3 - B^4X)}{120E\bar{I}B} \qquad (1)$$

Since only the parametric equation is needed, Eq. (1) is substituted by Eq. (2):

$$Y_{\text{Midline}} = K(-X^5 - aX^3 + X)$$

$$Y_{\text{Upper}} = Y_u + K_u(-X^5 - aX^3 + X)$$

$$Y_{\text{Lower}} = Y_L + K_L(-X^5 - aX^3 + X)$$

$$a = \frac{1 - B^4}{B^2} \qquad (2)$$

Smart flap geometry profile has not fixed in different angles of flaps(AOF). $K$ in Eq. (2) is a parameter so that it is changed in different AOFs.

The bending equation can be used for midline. For upper and lower flap surface, the configuration is manipulated by making minor modifications. The coefficients of Eq. (2) are determined by an iterative process. Each profile is visualized by using Fortran language program, and the value of the coefficient is either increased or decreased until the desired profile is obtained. A parametric smart airfoil is designed and a computational fluid dynamics simulation is done over them.

### B: Governing Equation for Fluid
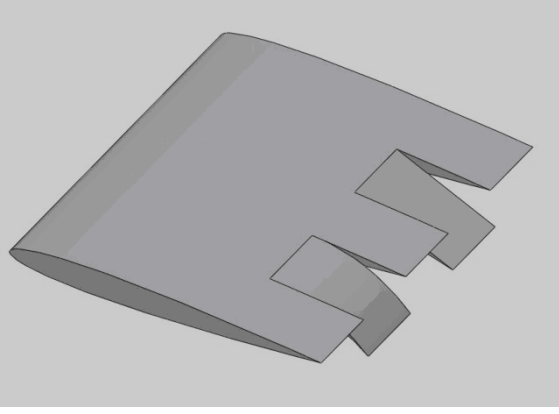The basic equations which describe the conservation of mass, momentum and scalar quantities can be
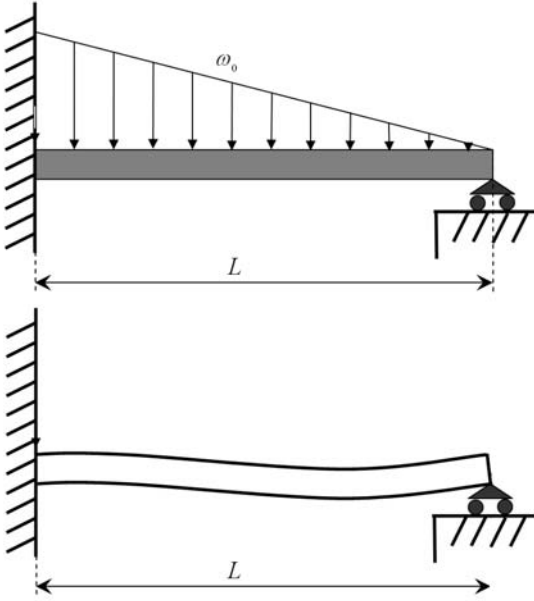
**Figure 1.** Smart and Convectional Flap.



**Figure 2.** Cantilever beam model.

expressed in the following vector form. They are independent on the used coordinate system.

$$\frac{\partial \rho}{\partial t} + div(\rho \tilde{\mathbf{V}}) = S_m \tag{3}$$

$$\frac{\partial (\rho \tilde{\mathbf{V}})}{\partial t} + div(\rho \tilde{\mathbf{V}} \otimes \tilde{\mathbf{V}} - \tilde{\mathbf{T}}) = \tilde{\mathbf{S}}_{\mathsf{v}} \tag{4}$$

$$\frac{\partial (\rho \phi)}{\partial t} + div(\rho \tilde{\mathbf{V}} \phi - \tilde{\mathbf{q}}) = \tilde{\mathbf{S}}_{\Phi} \tag{5}$$

The latter two are usually expressed in terms of basic dependent variables. The stress tensor for a Newtonian fluid is:

$$\vec{T} = -P\vec{I} + 2\mu \vec{D} \tag{6}$$

and the Fourier-type law usually gives the scalar flux vector:

$$\overrightarrow{q} = \Gamma_\phi \, grad\phi \tag{7}$$

For the purpose of illustration of Eq. (5), it may be expressed in 2D Cartesian coordinates as:

$$\overbrace{\frac{\partial (\rho \phi)}{\partial t}}^{transient\ term} + \overbrace{\frac{\partial (\rho u \phi)}{\partial x} + \frac{\partial (\rho v \phi)}{\partial y}}^{convection\ term} - \\ \underbrace{\frac{\partial}{\partial x}(\Gamma_\phi \frac{\partial \phi}{\partial x}) - \frac{\partial}{\partial y}(\Gamma_\phi \frac{\partial \phi}{\partial y})}_{diffusion\ term} = \overbrace{S_\phi}^{source} \tag{8}$$

$$\overbrace{\frac{\partial (\rho \phi)}{\partial t}}^{transient\ term} + \overbrace{\frac{\partial (\rho u \phi)}{\partial x} + \frac{\partial (\rho v \phi)}{\partial y}}^{convection\ term} - \\ \underbrace{\frac{\partial}{\partial x}(\Gamma_\phi \frac{\partial \phi}{\partial x}) - \frac{\partial}{\partial y}(\Gamma_\phi \frac{\partial \phi}{\partial y})}_{diffusion\ term} = \overbrace{S_\phi}^{source}$$

Turbulence is accounted for by adopting the $k - \epsilon$ turbulence model. The governing equations for these quantities are:

$$\frac{\partial}{\partial t}(\rho k) + \frac{\partial}{\partial x_j}(\rho u_j k - \Gamma_k \frac{\partial k}{\partial x_j}) = G - \rho \varepsilon \tag{9}$$

$$\frac{\partial}{\partial t}(\rho \varepsilon) + \frac{\partial}{\partial x_j}(\rho u_j \varepsilon - \Gamma_\varepsilon \frac{\partial \varepsilon}{\partial x_j}) = C_1 \frac{\varepsilon}{k} G - C_2 \rho \frac{\varepsilon^2}{k} \tag{10}$$

The turbulent viscosity and diffusivity coefficients are defined as:

$$\mu_t = C_\mu \rho \frac{k^2}{\epsilon} \tag{11}$$

$$\Gamma_\phi^t = (\frac{\mu_t}{\sigma_\phi^t}) \tag{12}$$

and the generation term G in Eqs. (6) and (7) is defined as:

$$G = \mu_t \left[ \left( \frac{\partial u_i}{\partial x_j} + \frac{\partial u_j}{\partial x_i} \right) \frac{\partial u_i}{\partial x_j} \right] \tag{13}$$

**C: Finite-Volume Discretization**

The discretization of the above differential equations is carried out by using a finite-volume approach. First, the solution domain is divided into a finite number of discrete volumes or cells, where all variables are stored at their geometric centers (see *e.g.* Figure 3).

The equations are integrated over all the control volumes by utilizing the Gaussian theorem. The discrete expressions are presented to refer to only one
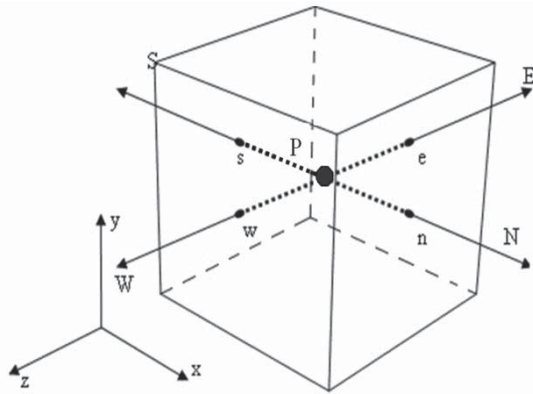
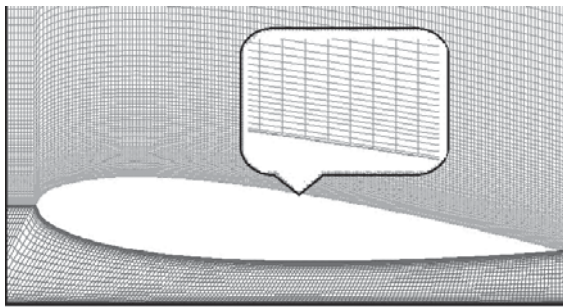**Figure 3.** Finite volume and storage arrangement.



**Figure 4.** grid topology and H grid.

face of the control volume, namely, $e$, for the sake of brevity. For any variable $\phi$ (which may also stand for the velocity components), the result of the integration yields:

$$\frac{\delta v}{\delta t}[(\rho\,\phi)_p^{n+1} - (\rho\,\phi)_p^n] + I_e - I_w$$
$$+ I_n - I_s = S_\phi\,\delta\,v \qquad (14)$$

where $I$s are the combined cell-face convection $I^C$ and diffusion $I^D$ fluxes. The diffusion flux is approximated by central differences and can be written for cell-face (e) of the control volume in Figure 3 as:

$$I_e^D = D_e(\phi_p - \phi_E) - S_e^\phi \qquad (15)$$

where $S_e^\phi$ stands for cross derivative arising from mesh nonorthogonality. The discretization of the convective flux requires special attention and it helps to develop the various schemes. A representation of the convective flux for cell-face (e) is:

$$I_e^c = (\rho.V.A)_e\,\phi_e = F_e\,\phi_e \qquad (16)$$

The value of $\phi_e$ is not known and it should be estimated from the values at neighboring grid points by interpolation. The expression for the $\phi_e$ is determined by the SBIC scheme [40], which is based on the NVD

technique using interpolation from the nodes E, P and W. The expression can be written as:

$$\phi_e = \phi_W + (\phi_E - \phi_W).\tilde{\phi}_e \qquad (17)$$

The functional relationship utilized in SBIC scheme for $\tilde{\phi}_e$ is illustrated in Figure 3 and is given as:

$$\tilde{\varphi}_e = \tilde{\varphi}_p, \quad IF\ \tilde{\varphi}_P \notin [0,1]$$

$$\tilde{\varphi}_e = -\frac{\tilde{x}_p - \tilde{x}_e}{\kappa\,(\tilde{x}_p - 1)}\tilde{\varphi}_p^2$$

$$+ \left(1 + \frac{\tilde{x}_p - \tilde{x}_e}{\kappa\,(\tilde{x}_p - 1)}\right)\tilde{\varphi}_p, \quad IF\ \tilde{\varphi}_P \in [0,\kappa]$$

$$\tilde{\varphi}_e = \frac{\tilde{x}_p - \tilde{x}_e}{\tilde{x}_p - 1} + \frac{\tilde{x}_p - 1}{\tilde{x}_p - 1}\tilde{\varphi}_p, \quad IF\ \tilde{\varphi}_P \in [\kappa,1] \qquad (18)$$

where

$$\tilde{\phi}_p = \frac{\phi_p - \phi_W}{\phi_E - \phi_W}, \qquad \tilde{\phi}_e = \frac{\phi_e - \phi_W}{\phi_E - \phi_W}$$

$$\tilde{x}_p = \frac{x_p - x_W}{x_E - x_W}, \qquad \tilde{x}_e = \frac{x_e - x_W}{x_E - x_W} \qquad (19)$$

The limits on the selection of $\kappa$ could be determined in the following way. Obviously, the lower limit is $\kappa = 0$, which would represent switching between upwind and central differencing. It is not favorable, because it is essential to avoid the abrupt switching between the schemes in order to achieve the converged solution. The value of $\kappa$ should be kept as low as possible in order to attain the maximum resolution of the scheme. The final form of the discretized equation from each approximation is given as:

$$A_P.\phi_P = \sum_{m=E,W,N,S} A_m.\phi_m + S'_\phi \quad + S_{dc} \qquad (20)$$

where $A$ s are the convection-diffusion coefficients. The term $S'_\phi$ in Eq. (20) contains quantities arising from non-orthogonality, numerical dissipation terms and external sources. For the momentum equations, it is easy to separate out the pressure-gradient source from the convected momentum fluxes. $S_{dc}$ is the contribution due to the adapted deferred correction procedure.
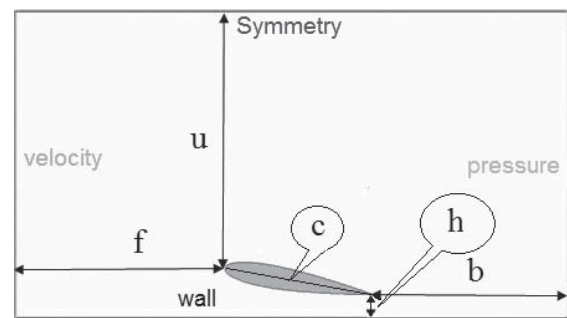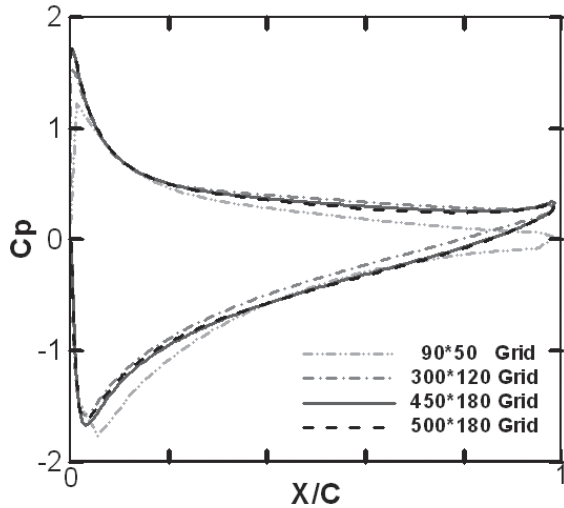


**Figure 5.** Dimension of domain.

**Figure 6.** Effect of grid sizing on pressure distribution on the surface of the airfoil for an angle of attack $10^{\circ}$ and $h/c = 0.2$.
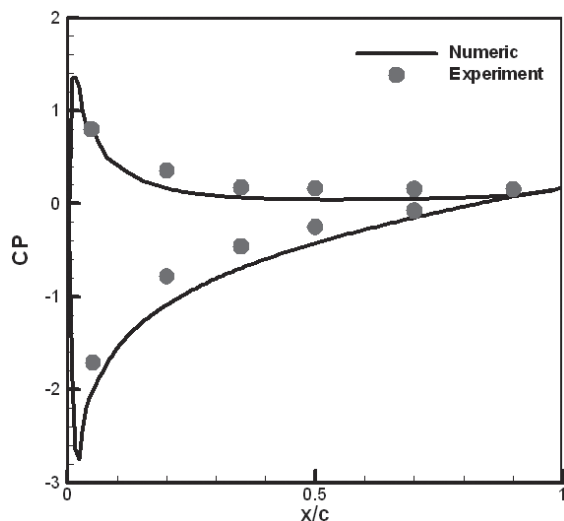


**Figure 8.** Comparison Numerical and Experimental distributions of mean velocity in the wake region. (a) $x/c = 0.5$ and (b) $x/c = 1$ from trailing edge for NACA0015, AOA=$5^{\circ}$ and $h/c = 0.1$.



**Figure 7.** Pressure coefficient distribution on the surface of the airfoil NACA 0015 for an AOA=$7.5^{\circ}$ and $h/c = 0.8$.



**Figure 9.** Convergence histories for x-velocity.

## GRID STRATEGY

The grid structure used in CFD simulation is created by a structured mesh employed because of its simplicity and applicability to the current flow configuration (*i.e.*, with a near-by ground). The schematic shape of these two-dimensional structured grids is shown in Figure 4.

According to Figure 5, the dimension of domain has been obtained after doing several various lengths for $b$, $f$, and $u$ and independent lengths have been chosen. The grid size is determined after the grid independence that is found by doing several different trials. For example, the effect of grid size is illustrated in Figure 6. For other cases, the above process is utilized for grid and domain independences.
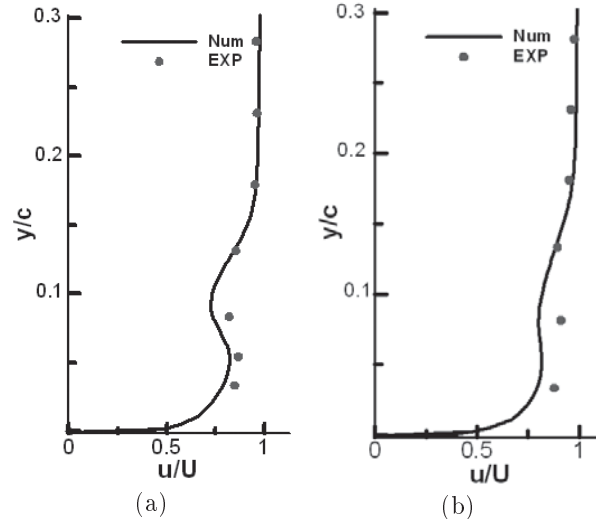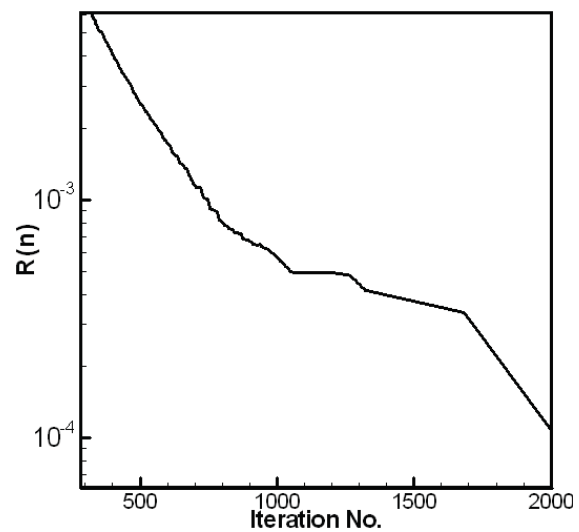
## BOUNDARY CONDITIONS

Figure 5 manifests the boundary condition. At the inlet, velocity has been prescribed. At the outlet, the pressure is fixed. Slip boundary conditions are used on the upper walls of the domain and wall boundary conditions are applied for airfoil surface and ground surface. So, the non-slip condition is utilized at the solid walls. To account for the steep variations in turbulent boundary layers near solid walls, wall function are employed which define the velocity profile in the vicinity of no-slip boundaries.
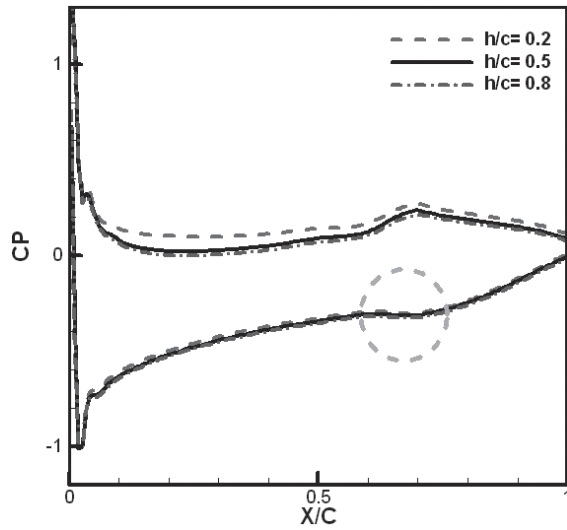
**Figure 10.** Pressure coefficient distribution on the surface of the smart airfoil for AOF= -7.5°.
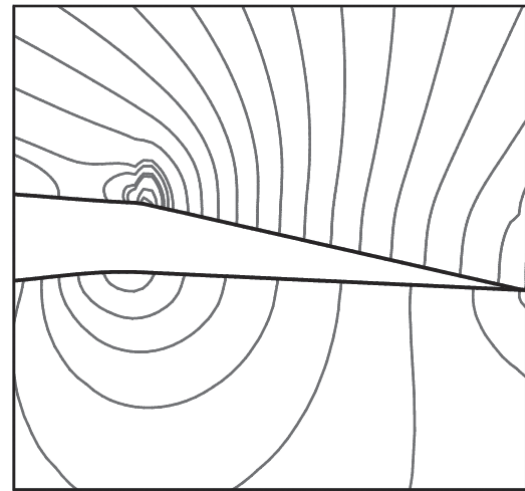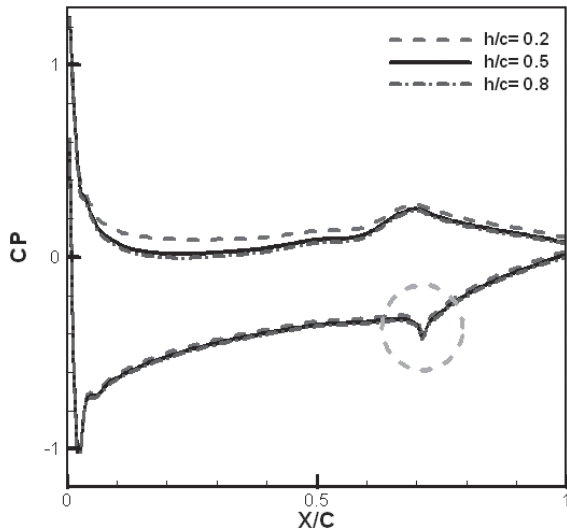


**Figure 11.** Pressure coefficient distribution on the surface of the conventional airfoil for AOF=7.5°.

## RESULTS AND DISCUSSION

The results are presented and discussed in this section. Table 1 shows the setting for numerical simulation. At first, the simulation of the flow around the airfoil NACA0015 has been performed. Then, the numerical investigation of the flow around the airfoil NACA0009 with smart and conventional flaps have been done, and the effects of flap length, angle of flap and ground clearance are discussed.

The simulation is two-dimensional. The ressure coefficient distribution, the lift and drag coefficients of airfoil have been analyzed. The Reynolds number of this study is $2.4 \times 10^5$. This number indicates that the airflow has full turbulent regions.

The numerical and experimental pressure coef-



**Figure 12.** Contours of pressure coefficient distribution on the surface of the smart airfoil for an AOF=-7.5° and $h/c = 0.5$.
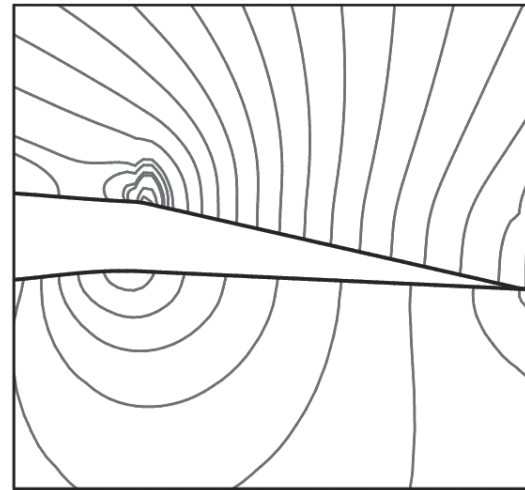


**Figure 13.** Contours of pressure coefficient distribution on the surface of the conventional airfoil for an AOF=-7.5° and $h/c = 0.5$.

ficient distribution on the surface of the airfoil for AOA=7.5° and $h/c = 0.8$ is compared in Figure 7. It can be seen that there is a good agreement between present numerical and experimental data [2]. Table 2 also shows lift and drag coefficients in numerical and experimental data. Figure 8 illustrates the velocity profile behind the airfoil at $x/c = 0.5$ and $x/c = 1$ from trailing edge in AOA=$5^o$ and $h/c = 0.1$. The numerical results are in good agreement with the experiment.

**Table 1.** Settings for Numerical Simulation.

| Flow | turbulent |
|---|---|
| Precision | 2-D Double Precision |
| Scheme | Normalize variable diagram |
| Solver | SIMPLE |
| turbulent model | |

The difference between experimental and numerical in drag coefficient is shown in Table 2. This difference can be due to turbulence models, because the reference [9, 11] has also reported this problem.

Usually, there are two parts of iterations, inner iterations and outer ones. In the inner part, linear equations of momentum and scalar are solved by a strongly implicit procedure (SIP) and pressure-correction equations are solved by Biconjugate gradient method. For the outer part, the iteration is terminated according to a fractional change criterion typically of the form:

$$R(n) = \max \left( \left| \frac{\phi^n - \phi^{n-1}}{\phi_{ref}} \right| \right) \leq \varepsilon \qquad (21)$$

where $\phi_{ref}$ is reference value for $\phi$ (which may also stand for the velocity components), $\varepsilon$ is a small number and $n$ is an iteration counter. In this work, $\varepsilon$ value is used in the range $10^{-6}$-$10^{-5}$. Convergence history is shown in Figure 9. The figure manifests that the convergence criterion is satisfied.

The airfoil NACA0009 is selected in this study. The simulation method for this test case is the same as the previous one. The airflow treatment and the effect of smart and conventional flap in ground proximity are investigated.

**Table 2.** Comparison of lift and drag coefficients for airfoil NACA0015 for AOA=5°.

| | | CL | CD |
|---|---|---|---|
| $h/c = 0.1$ | Experiment | 0.672 | 0.0136 |
| | Numeric | 0.620 | 0.0133 |
| c=0.5 | Experiment | 0.586 | 0.0143 |
| | Numeric | 0.556 | 0.0176 |
| h/c=0.8 | Experiment | 0.520 | 0.0148 |
| | Numeric | 0.500 | 0.0230 |
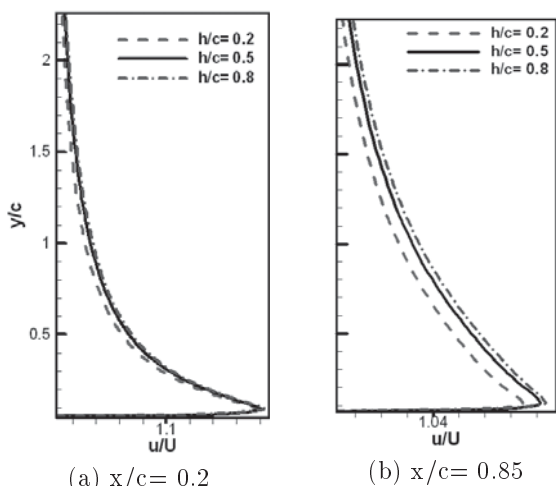


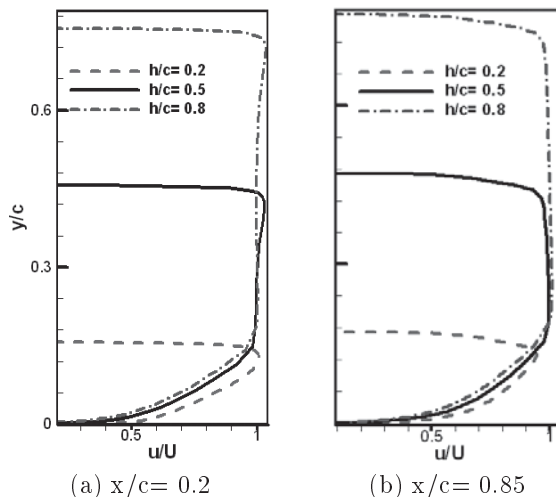**Figure 14.** Velocity profile in upper surface of smart airfoil for AOF=-5°.



(a) x/c= 0.2          (b) x/c= 0.85

**Figure 15.** Velocity profile in lower surface of smart airfoil for AOF=-5°.

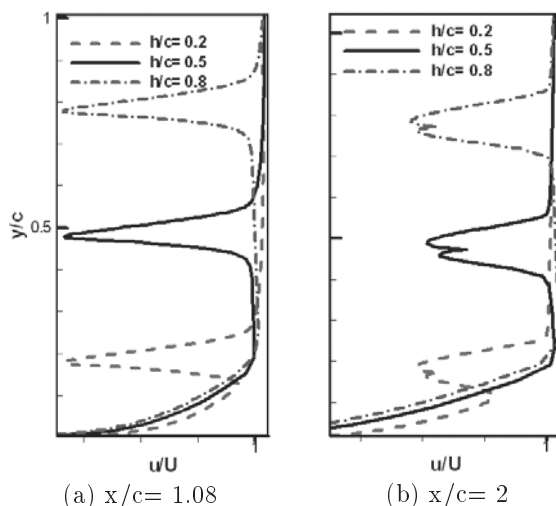

(a) x/c= 1.08          (b) x/c= 2

**Figure 16.** Velocity profile in behind the airfoil for AOF=-5°.

Figures 10 and 11, respectively, illustrate the pressure coefficient distribution on the airfoil surface in AOF=-7.5°. It can be observed that the pressure coefficient distribution on the suction side and the pressure side increases as reduction ground clearance in both smart and conventional flaps. The zones marked with a circle are showed in Figures 12 and 13. This zone is the junction region of flap to the airfoil. These figures indicate the sudden change in the pressure coefficient distribution on the upper surface of the airfoil with conventional flap while it is smooth for smart case. This sudden change is due to the sharp change of the airfoil surface in the junction zone in the conventional airfoil. Figures 12 and 13 prove the pressure contour of the discussed cases and they show more pressure changes in the junction of flap with
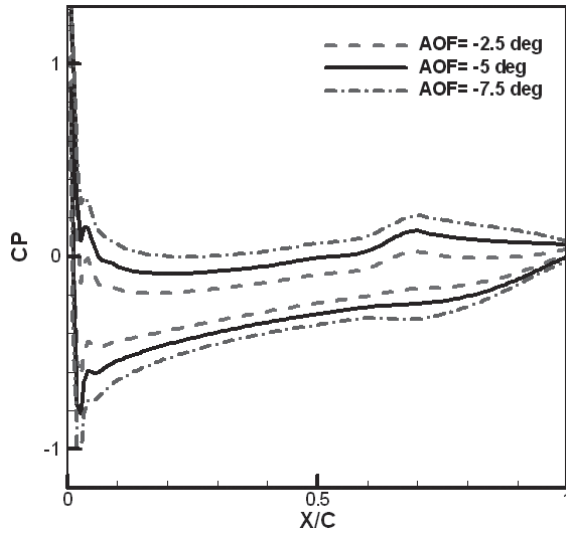
**Figure 17.** Pressure coefficient distribution on the surface of the smart airfoil for h/c=0.8.
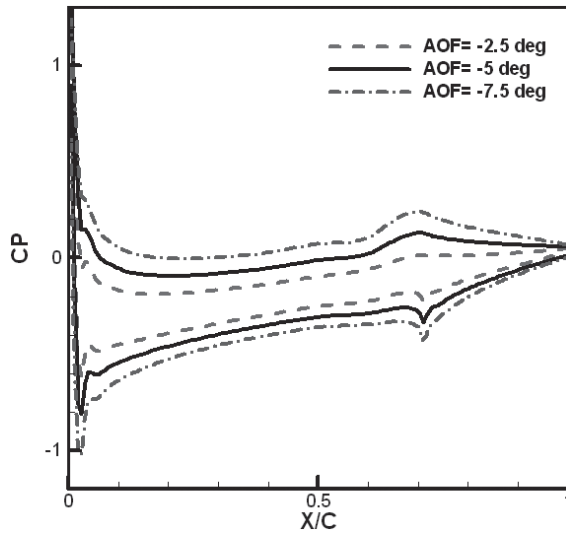


**Figure 18.** Pressure coefficient distribution on the surface of the conventional airfoil for h/c=0.8.

airfoil in the conventional flap that is in agreement with the previous results. It is considerable that the discussed phenomenon has not happened in the smart airfoil. This is one of advantage of smart technology in airfoils. Table 3 illustrates lift and drag coefficients and L/D.

The comparisons prove that the lift coefficient of the smart flap is more than that of the conventional flap for all different ground clearance and drag coefficients have reverse treatment. Also, the L/D ratio of the smart flap is higher than that of the conventional flap. These results indicate that the reduction of ground clearance leads to an increase in lift coefficient, decrease in drag coefficient and it results in L/D increase.

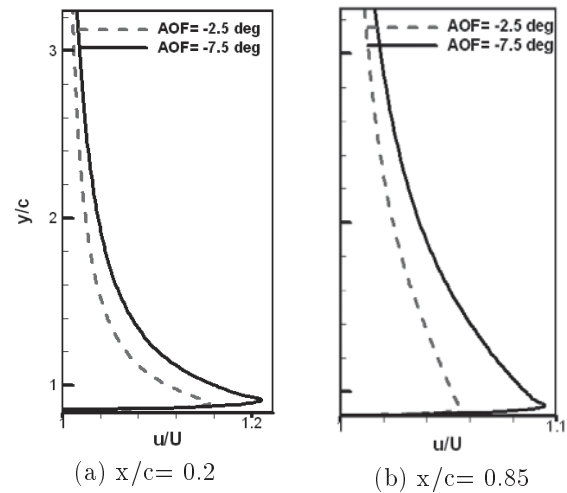Figure 14 manifests velocity profiles on the upper



(a) x/c= 0.2                    (b) x/c= 0.85

**Figure 19.** Velocity profile in upper surface of smart airfoil for h/c=0.8.

surface of airfoil at x/c= 0.2 and x/c=0.85 for AOF=-5° and different ground clearance. The comparisons prove that the velocity on the upper surface of the airfoil decreases slightly as low ground clearance. Also, it can be observed that the difference of velocity in x/c=0.85 (flap zone) is higher than x/c=0.2. As a result of this, the ground effect has more effect on velocity in the flap zone. Air flow is incarcerated near the leading edge by decreasing ground clearance, pressure has increased and velocity has decreased. The velocity reduction has impressed the downstream on the upper surface of the airfoil. Figure 15 shows that velocity in the lower surface has decreased slightly with ground clearance and pressure has increased, but this increase is more than the pressure increase on the upper surface of the airfoil and the lift to drag ratio has increased with the reduction of ground clearance.

Figure 16 illustrates the wake flow profile behind the airfoil for AOF=-5° and two distances from trailing

**Table 3.** Lift (a) and drag (b) coefficients and lift - drag ratio(c) for smart and conventional airfoils for AOF= -7.5°.

| h/c | Smart Flap | Convection Flap |
|-----|-----------|-----------------|
| 0.2 | 0.531 | 0.512 |
| 0.5 | 0.500 | 0.485 |
| 0.8 | 0.490 | 0.478 |
| (a) | | |

| h/c | Smart Flap | Convection Flap |
|-----|-----------|-----------------|
| 0.2 | 0.0292 | 0.0296 |
| 0.5 | 0.0300 | 0.0306 |
| 0.8 | 0.0306 | 0.0312 |
| (b) | | |

| h/c | Smart Flap | Convection Flap |
|-----|-----------|-----------------|
| 0.2 | 18.2 | 17.3 |
| 0.5 | 16.7 | 15.8 |
| 0.8 | 16.0 | 15.3 |
| (c) | | |

(a) x/c= 0.2                        (b) x/c= 0.85

**Figure 20.** Velocity profile in lower surface of smart airfoil at h/c=0.8.



(a) x/c= 0.2                        (b) x/c= 0.85
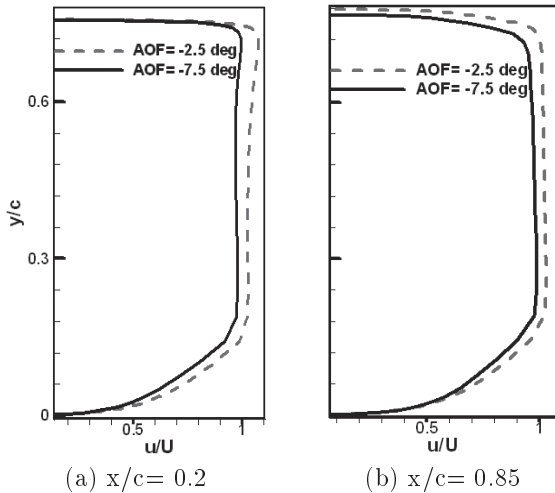
**Figure 21.** Comparison smart and conventional flap by velocity profile in upper surface of airfoil at $h/c = 0.2$, AOF=-7.5°.

edge. This figure shows that decreasing distance does not have any effect on wake flow behind the airfoil. The other phenomena seen in Figure 16 means that the velocity in the boundary layer on the ground has increased with the reduction of ground clearance.

Figures 17 and 18, respectively, show the pressure coefficient distribution on the surface of smart and conventional airfoils for $h/c = 0.8$ and AOF= -2.5⁰, -5⁰, -7.5⁰. The comparison proves that pressure has increased on the pressure side and has decreased on the suction side as the angle of flap becomes more. This phenomenon happens, because the pressure is increased on the lower part as creating a barrier by increasing angle of flap. On the other hand, the large deflection of the flap has created a larger barrier in the path flow, has caused increasing pressure in the lower surface of the flap, has affected the pressure of the lower surface, and has increased it. Flow velocity on the suction side is increased due to the increased curvature of the upper surface of the airfoil and as for these results, its pressure is reduced. The pressure reduction is extended to all of the upper surface of the airfoil as a result of the increasing angle of the flap. The lift and drag coefficients and L/D are shown in Table 4 for smart and conventional flaps. The comparison of these results proves that the L/D is higher in smart case.

Figures 19(a) and (b) illustrate velocity profiles on the upper surface of the airfoil. The comparison proves that the flow velocity on the upper surface of the airfoil at the AOF=-7.5⁰ is more than AOF=-2.5⁰. This phenomenon has been observed, because the curvature of the upper surface of the airfoil is larger and its speed is higher in this area-section. Table 5 represents that the flow rate passing through the lower surface of the airfoil is reduced as the angle of flap is increased. In this test, area-section is fixed from the leading edge to the first of flap for both flap angles. When the angle
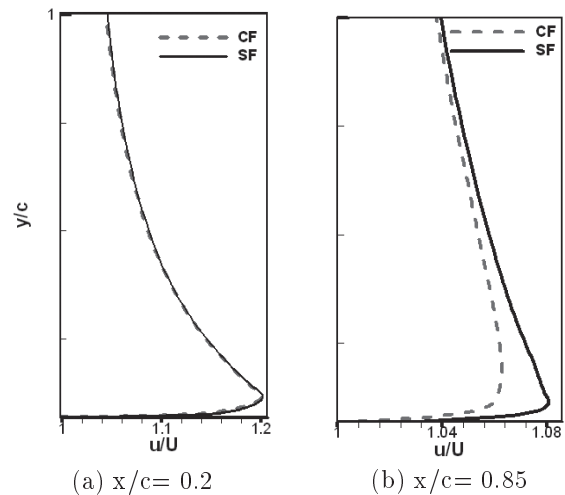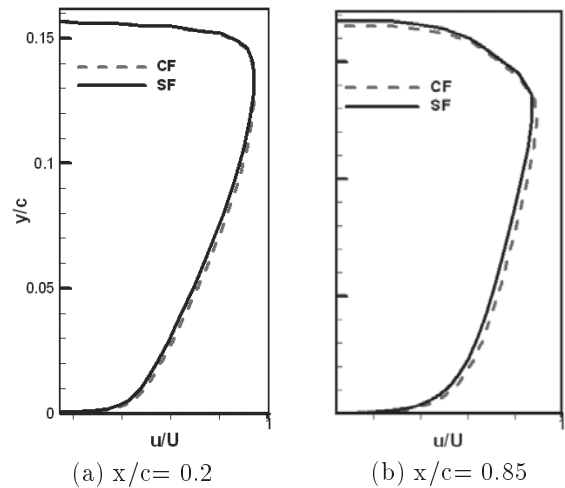


(a) x/c= 0.2                        (b) x/c= 0.85

**Figure 22.** Comparison smart and conventional flap by velocity profile in lower surface of airfoil at $h/c = 0.2$, AOF=-7.5°.

**Table 4.** Lift (a) and drag (b) coefficient and lift - drag ratio(c) for smart and conventional airfoils for h/c=0.8.

| AOF (deg) | Smart Flap | Convection Flap |
|---|---|---|
| -2.5 | 0.178 | 0.177 |
| -5 | 0.337 | 0.332 |
| -7.5 | 0.490 | 0.478 |

(a)

| AOF (deg) | Smart Flap | Convection Flap |
|---|---|---|
| -2.5 | 0.0288 | 0.0298 |
| -5 | 0.0299 | 0.0305 |
| -7.5 | 0.0306 | 0.0312 |

(b)

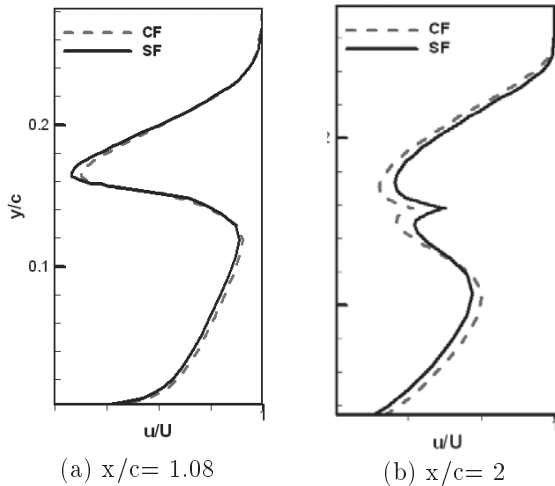| AOF (deg) | Smart Flap | Convection Flap |
|---|---|---|
| -2.5 | 6.19 | 5.94 |
| -5 | 11.3 | 10.9 |
| -7.5 | 16.0 | 15.3 |

(c)

(a) x/c= 1.08       (b) x/c= 2

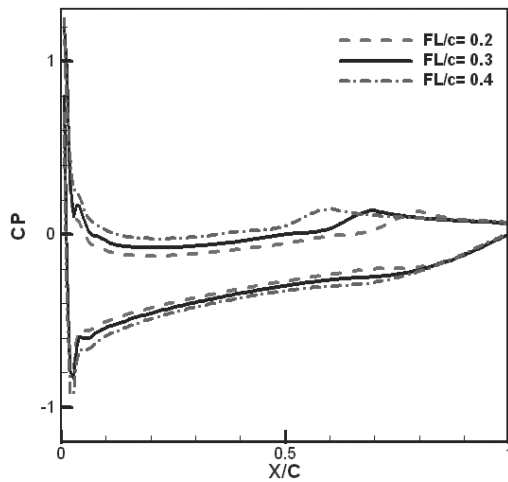**Figure 23.** Comparison smart and conventional flap by velocity profile in behind the airfoil at h/c=0.2, AOF=-7.5°.



**Figure 24.** Pressure coefficient distribution on the surface of the smart airfoil for h/c=0.5 and AOF=-5°.

of flap is increased, the passing flow rate between the ground surface and the lower surface of the airfoil is decreased. As for these results, the passing flow rate from the upper surface of the airfoil is increased by increasing the angle of flap and the pressure in the suction side, from the leading edge to the beginning of flap, is less in AOF=-7.5°.

Velocity profiles on the lower surface of the airfoil for both $x/c = 0.2$ and $x/c = 0.85$ and ground clearance $h/c = 0.8$ has been shown in Figure 20. The comparison of profiles in the AOF=-2.5⁰, -7.5⁰

**Table 5.** Volume flow rate passing between lower surface of airfoil and ground for smart airfoil and h/c=0.8.

| AOF | Volume flow rate |
|-----|------------------|
| -2.5 | 2.560 |
| -7.5 | 2.404 |

demonstrates that the velocity in the AOF=-7.5⁰ is less than AOF=-2.5⁰. The reduction of velocity redounds to increase pressure on the lower surface of the airfoil.

Figures 21, 22 and 23 show the comparison between the smart and conventional flaps in ground clearance $h/c = 0.2$. The comparison velocity profiles have been considered at AOF=-7.5⁰. Figure 21 is related to the velocity profiles at the upper surface of the airfoil that has been drawn in two different sections. Velocity profiles have no significant difference at the beginning of the airfoil between the conventional and smart flaps, but velocity has more growth rate in the smart flap; therefore, pressure for the smart flap is less than that of the conventional flap in this section. Figure 22 proves the velocity profile on the lower surface of the airfoil. There is no difference between the smart and conventional flaps in these two sections. Figure 23 demonstrates the velocity profile behind the airfoil. In the case of the smart flap, the created wake behind airfoils is smaller, so the drag is smaller than that of the conventional flap.

Figure 24 shows the effect of various flap lengths on pressure coefficient distribution on the surface of the smart airfoil for h/c=0.5 and AOF=-5°. Three different flap lengths FL/c=0.2,0.3,0.4 are considered. As indicated in this figure, the increasing of flap length lead to the increasing of pressure coefficient on the pressure side and decreasing pressure coefficient in the suction side. In addition, Table 6 manifests the lift and drag coefficients and the L/D of these cases. It illustrates that lift and drag coefficients are slightly increased with flap length and L/D is increased, too. Figure 25 demonstrates velocity profiles on the upper surface of the smart airfoil for different flap lengths in h/c=0.5 and AOF=-5°. This result represents that the velocity on the upper surface of the airfoil is increased
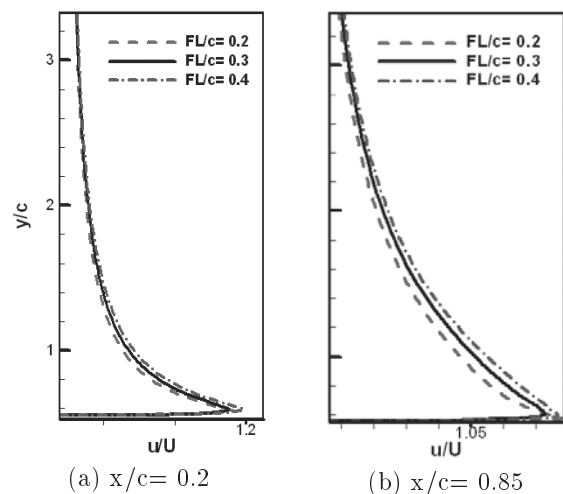


(a) x/c= 0.2       (b) x/c= 0.85

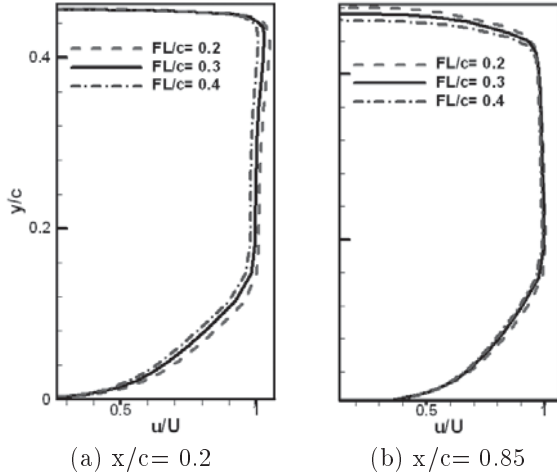**Figure 25.** Velocity profile in upper surface of smart airfoil at h/c=0.5, AOF=-5°.

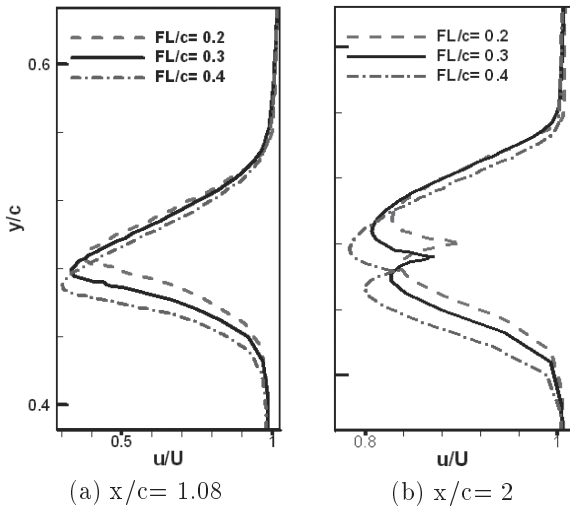Figure 26. Velocity profile in lower surface of smart airfoil at h/c=0.5, AOF=-5°.



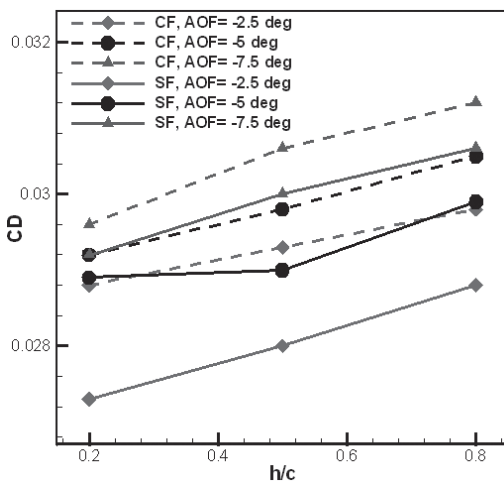Figure 27. Velocity profile in behind the smart airfoil at h/c=0.5, AOF=-5°.



Figure 28. Variations in CD as a function of h/c for smart and conventional flap and different angle of flap.
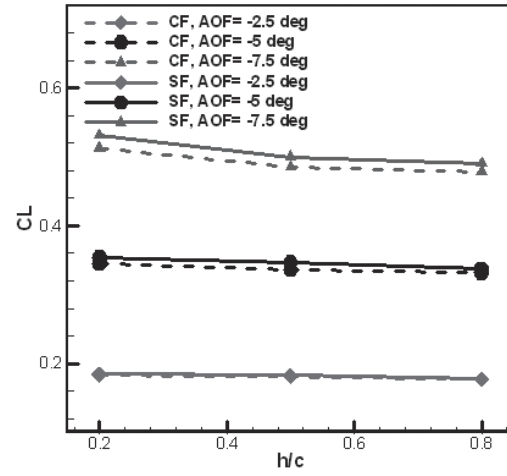


Figure 29. Variations in CL as a function of h/c for smart and conventional flap and different angle of flap.
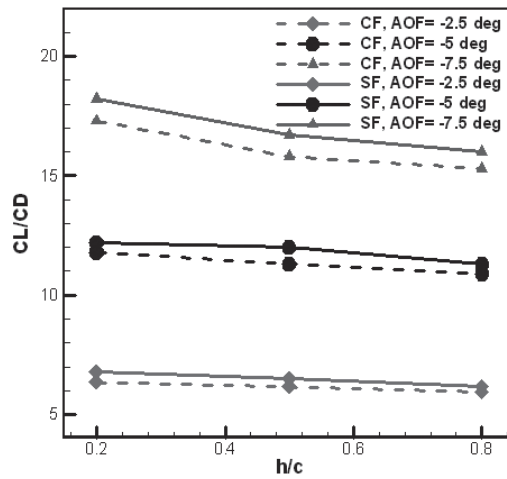


Figure 30. Variations in L/D as a function of h/c for smart and conventional flap and different angle of flap.

slightly as flap length is increased. Figure 26 proves the velocity profile on the lower surface of the airfoil. The velocity profile behind the airfoil in different flap lengths has been plotted in Figure 27. It can be seen that the wake flow behind the airfoil with larger flap length is stronger and it leads to a higher drag coefficient.

Lift and drag coefficients and L/D ratio are shown in Figures 28, 29 and 30, respectively. Figures 28 and 29 prove that the drag coefficient is decreased and the lift coefficient is increased with reduction of ground clearance. Thus, the L/D ratio is increased with the reduction of ground clearance.

## CONCLUSION

The smart flap of airfoil under the ground effect is carried out by integration of CFD. A parametric bending profile of a smart flap is designed considering different

**Table 6.** Lift and drag coefficients and lift - drag ratio for smart airfoils for h/c=0.5 , AOF=-5°.

| FL/c | CL | CD | L/D |
|------|-------|--------|------|
| 0.2 | 0.282 | 0.0264 | 10.7 |
| 0.3 | 0.347 | 0.0289 | 12.0 |
| 0.4 | 0.413 | 0.0293 | 14.1 |

types of beams. A cantilever beam with a uniformly varying load with roller support at the free end is considered here. A pressure-based implicit procedure is utilized to solve Navier-Stokes equations. The SIMPLE algorithm is applied for turbulent aerodynamic flows around airfoils with smart and conventional flaps in different flap lengths, flap angles and ground clearance. The main findings can be summarized as follows: 1- The agreement between the presented prediction and the experimental data is considerable; 2- The pressure coefficient distribution in the smart flap is smoother than that of the conventional flap; 3- The lift-drag ratio in smart flap is higher than that of the conventional flap; 4- The maximum lift-drag ratio is at attack angle 7.5° 5- The minimum ground clearance has the highest lift-drag ratio; and 6- The increasing of flap length leads to increase in lift-drag ratio.

### REFERENCES

1. Ahmed M., Ali S.H., Imran G.M. and Sharma S.D., "Experimental Investigation of the Flow Field of a Symmetrical Airfoil in Ground Effect", *Presented at the 21st Applied Aerodynamics Conference*, (2003).

2. Ahmed M. and Sharma S., "An Investigation on the Aerodynamics of a Symmetrical Airfoil in Ground Effect", *Experimental Thermal and Fluid Science*, **29**, PP 633-647(2005).

3. Ahmed M., Takasaki T., and Kohama Y., "Experiments on the Aerodynamics of a Cambered Airfoil in Ground Effect", *Presented at the 44th AIAA Aerospace Sciences Meeting and Exhibit*, Reno, Nevada, (2006).

4. Kliment L. and Rokhsaz K., "Experimental Investigation of Pairs of Vortex Filaments in Ground Effect", *Journal of Aircraft*, **45**, PP 622(2008).

5. Takahisa M., Takuma K., Shuya Y., and Yasuaki K., "Study of Unsteady Characteristics of Wings in Ground Effect", *Presented at the Third International Symposium on Transdisciplinary Fluid Integration*, Matsushima, Miyagi, Japan, (2006).

6. Zerihan J. and Xin Z., "Aerodynamics of a Single Element Wing in Ground Effect", *Journal of Aircraft*, **37**, PP 1058-1064(2000).

7. Nazarinia M., Soltani M.R., and Ghorbanian K., "Experimental Study of Vortex Shapes Behind a Wing Equipped with Different Winglets", *Journal of Aerospace Science and Technology (JAST)*, **3**, PP 1-15(2006).

8. Jung K., Chun H., and Kim H., "Experimental Investigation of Wing-in-Ground Effect with a NACA6409 Section", *Journal of Marine Science and Technology*, **13**, PP 317-327(2008).

9. Smith J., "Computational Analysis of Airfoils in Ground Effect for Use as a Design Tool", *Master Science of Aerospace Engineering*, West Virginia University, (2007).

10. Smith J., Graham H. and Smith J., "The Validation of an Airfoil in the Ground Effect Regime Using 2-D CFD Analysis", *Presented at the 26th AIAA Aerodynamic Measurement Technology and Ground Testing Conference*, Seattle, Washington, (2008).

11. Vu P., "CFD Study of Wing Tip Vortices for Inverted Airfoils in Ground Effect", MS Thesis, School of Engineering, Cranfield University, (2006).

12. Park K. and Lee J., "Influence of Endplate on Aerodynamic Characteristics of Low-Aspect-Ratio Wing in Ground Effect", *Journal of Mechanical Science and Technology*, **22**, PP 2578-2589(2008).

13. Abramowski T., "Numerical Investigation of Airfoil in Ground Proximity", *Journal of Theoretical and Applied Mechanics*, **45**, PP 425(2007).

14. Moon Y., Oh H. and Seo J., "Aerodynamic Investigation of Three-Dimensional Wings in Ground Effect for Aero-Levitation Electric Vehicle", *Aerospace Science and Technology*, **9**, PP 485-494(2005).

15. Kim H., Chun H. and Jung K., "Aeronumeric Optimal Design of a Wing-in-Ground-Effect Craft", *Journal of Marine Science and Technology*, **14**, PP 39-50(2009).

16. Park K., Kim B., Lee J. and Kim K., "Aerodynamics and Optimization of Airfoil Under Ground Effect", *International Journal of Mechanical Systems Science and Engineering*, **1**, (2009).

17. Boschetti P., Cardenas E., Amerio A. and Arevalo A., "Stability and Performance of a Light Unmanned Airplane in Ground Effect", *Presented at the 48th AIAA Aerospace Sciences Meeting Including the New Horizons Forum and Aerospace Exposition*, Florida, (2010).

18. Juhee L., Chol-Ho H., Sam K.B., Kyoungwoo P. and Kwan A.J., "Optimization of Wings in Ground Effect Using Multi- Objective Genetic Algorithm", *Presented at the 48th AIAA Aerospace Sciences Meeting Including the New Horizons Forum and Aerospace Exposition*, Florida, (2010).

19. Xin Z. and Jonathan Z., "Aerodynamics of a Double Element Wing in Ground Effect", *Presented at the 40th AIAA Aerospace Sciences Meeting and Exhibit*, Reno, Nevada, (2002).

20. Moryoseff Y. and Levy Y., "Computational study of the Flow about an Oscillating Wing in Ground Effect", *AIAA Journal*, **43**, PP 863(2001).

21. Jones K., Bradshaw C., Papadopoulos J. and Platzer M., "Bio-Inspired Design of Flapping-wing Micro Air Vehicles", *Aeronautical Journal*, **109**, PP 385-394(2005).

22. Willis D., Peraire J. and Breuer K., "A Computational Investigation of Bio-Inspired Formation Flight and Ground Effect", *presented at the 25th AIAA Applied Aerodynamics Conference*, (2007).

23. Kamali R. and Rezaei Ravesh S., "Numerical Analysis of MAV's Flapping Wings in Unsteady Conditions", *Journal of Aerospace Science and Technology (JAST)*, **5**, PP 1-11(2008).

24. Bolonki A. and Gilyard G., "Estimated Benefits of Variable-Geometry Wing Camber Control for Transport Aircraft", *NASA TM-1999-206586*, (1999).

25. Jou P. N. and Jacob J. D., "Wake Vortex Mitigation Using Adaptive Airfoils", *American Institute of Aeronautics and Astronautics (AIAA)*, **57**, PP 167-176(1999).

26. Kudva J., Martin C., Jardine A., Sendeckyj G., Harris T., McGowan A. and Lake R., "Design, Fabrication, and Testing of the DARPA/Wright Lab "Smart Wing" Wind Tunnel Model", *Journal of American Institute of Aeronautics and Astronautics (AIAA)*, (1997).

27. Forster E., Sanders B. and Eastep F., "Synthesis of a Variable Geometry Trailing Edge Control Surface", *AIAA journal*, **1717**, (2003).

28. Florance J., Burner A., Fleming G., Hunter C., Graves S. and Martin C., "Contributions of the NASA Langley Research Center to the DARPA/AFRL/NASA/Northrop Grumman Smart Wing Program", *Presented at the 44th AIAA /ASME /ASCE/AHS Structures, Structural Dynamics, and Materials, Conference*, Virginia, (2003).

29. Quackenbush T., Carpenter B. and Gowing S., "Design and Testing of a Variable Geometry Ducted Propulsor Using Shape Memory Alloy Actuation", *Presented at the 43th AIAA Aerospace sciences Meeting and Exhibit*, Reno, Nevada, (2005).

30. Anusonti-Inthra P., Gandhi F. and Frecker M., "Design of a Conformable Rotor Airfoil Using Distributed Piezoelectric Actuation", *AIAA Journal*, **8**, PP 1684-1695(2005).

31. Tiseo B. and Koopmann G., "Smart Tunable Dynamic Vibration Absorbers", *Presented at the 12th AIAA/ CEAS Aeroacoustics Conference (27th AIAA Aeroacoustics conference)Smart Tunable Dynamic Vibration Absorbers*, Cambridge, Massachusetts, (2006).

32. Barlas T. and van Kuik G., "Review of State of the Art in Smart Rotor Control Research for Wind Turbines", *Progress in Aerospace Sciences*, **46**, PP 1-27(2010).

33. Campanile L. and Anders S., "Aerodynamic and Aeroelastic Amplification in Adaptive Belt-Rib Airfoils", *Aerospace Science and Technology*, **9**, PP 55-63(2005).

34. Chinnasamy P. and Chen Y., *Application of Computational Fluid Dynamics on Smart Wing Design*, University of Nevada, Las Vegas, (2005).

35. Matsuzaki Y. and Torii H., "Flutter Boundary Prediction of an Adaptive Smart Wing during Process of Adaptation Using Steady-State Response Data", *Presented at the 47th AIAA/ASME/ASCE/AHS Structures, Structural Dynamics, and Materials Conference*, Rhode Island, (2006).

36. Majji M., Rediniotis O., and Junkins J., "Design of a Morphing Wing: Modeling and Experiments", *Presented at the AIAA Atmospheric Flight Mechanics Conference and Exhibit*, South Carolina, (2007).

37. Abdullah E., Bil C. and Watkins S., "Application of Smart Materials for Adaptive Airfoil Control", *Presented at the 47th AIAA Aerospace Sciences Meeting Including The New Horizons Forum and Aerospace Exposition*, Orlando, Florida, (2009).

38. Wickramasinghe V., Chen Y., Martinez M., Kernaghan R. and Wong F., "Design and Verification of a Smart Wing for an Extremely-Agile Micro-Air-Vehicle", *American Institute of Aeronautics and Astronautics*, (2009).

39. Abdullah E., Bil C. and Watkins S., "Numerical Simulation of an Adaptive Airfoil System using SMA Actuators", *presented at the 48th AIAA Aerospace Sciences Meeting Including the New Horizons Forum and Aerospace Exposition*, (2010).

40. Djavareshkian M., Esmaeli A. and Parsani A., "Aerodynamics of Smart Flap Underground Effect", *Aerospace Science and Technology*, Article in Press, (2011).

41. Maghrebi M.J. and Soria J., "Outflow Boundary Condition Issues in Direct Numerical Simulation of Three-Dimensional Plane Wake Flow", *Journal of Aerospace Science and Technology (JAST)*, **3**, PP 177-183(2006).

42. Djavareshkian M., "A New NVD Scheme in Pressure-Based Finite-Volume Methods", *Presented at the 14th Australasian Fluid Mechanics Conference*, Adelaide, Australia, (2001).